PAPER

Local lattice distortions in oxygen deficient Mn-doped ZnO thin films, probed by electron paramagnetic resonance

Michael Lorenz,* Rolf Böttcher, Stefan Friedländer, Andreas Pöppl, Daniel Spemann† and Marius Grundmann

The structure and functional properties of metal oxide films for device applications are largely affected by oxygen vacancies. While the macroscopic relationship between functionality and oxygen supply during growth is easy to access, the local influence of changing oxygen content on the incorporated metal atoms has been rarely investigated. As a model system, we use Mn as a local probe in hetero- and homoepitaxial ZnO thin films for electron paramagnetic resonance (EPR). Mn is expected to be incorporated as Mn^{2+} in the Zn-lattice site of ZnO films grown in a wide range of oxygen partial pressures. The zero field splitting (ZFS) parameter D depends on the crystallographic c/a ratio of ZnO : Mn lattice constants as it measures the trigonal distortion of oxygen tetrahedra at the Zn^{2+} site with respect to the Mn^{2+} site. The ZFS parameter D correlates linearly with displacement of Mn^{2+} ions along the c-axis in the MnO_4 tetrahedra and the corresponding bond lengths between the Mn^{2+} ions and the axial oxygen ion.

1. Introduction

Oxide materials, in particular oxide thin films, gain more and more attention from both basic and applied points of view, due to interesting phenomena such as strong electron correlations and transparent oxide electronics. The functional properties of metal oxide thin films may be controlled by tuning the preparation conditions. However, in the interplay of structure, morphology and the functional properties such as conductivity or the ferroic properties, often an oxygen deficient growth environment is chosen because of the requirements of a smooth surface and an interface.[1] In pulsed laser deposition (PLD), one of the most flexible growth methods of oxide thin films,[2] the oxygen partial pressure during growth controls the distribution of oxygen vacancies.[3] Thus, oxygen vacancies are a common phenomenon in functional oxides, due to the often used oxygen deficient growth conditions. The effect of oxygen vacancies on structures and macroscopic functional properties is a highly interesting and current topic of interest, as the following examples show.

In the high-T_c superconductor $Y_1Ba_2Cu_3O_{7-\delta}$, under-doped surfaces with ordered oxygen vacancies result in an *ortho*-II band folding of the Fermi surface.[4] Detailed point defect analysis using both computational modeling and PLD growth of $SrTiO_3$ shows that precise growth control allows tuning of the

concentration of anion and cation vacancies and tailoring the performance of doped perovskite films.[5] Borisevich *et al.* report on the increasing consideration of "oxygen vacancies… to play a role in phenomena observed at transition-metal oxide interfaces".[6] There, cation displacements are observed at $SrRuO_3$/$La_{0.7}Sr_{0.3}MnO_3$ (LSMO) interfaces, indicating interface dipoles between the two metallic oxides. Magnetic exchange bias and coercive fields in $LSMO/SrTiO_3$ were found to increase with decreasing oxygen growth pressure in PLD and sputtering, thus opening a route for tuning exchange bias by the oxygen vacancy concentrations.[7] Detailed structural and X-ray photoelectron spectroscopy on LSMO revealed clear correlations of structural, electronic and transport properties with oxygen vacancy concentration from 0 to about 7%.[8] Other recent experimental examples are the effect of oxygen vacancies on resistive switching in TiO_{2-x} films[9] and on the two-dimensional electron gas at the $SrTiO_3$ surface.[10] In addition, first principle and density functional theory investigations have been performed on native point defects in $LaAlO_3$,[11] on magnetic properties of Mg doped $BiFeO_3$ with and without oxygen vacancies,[12] and on energetics of intrinsic defects and their complexes in ZnO.[13] Lany and Zunger calculated the donor level energy of the oxygen vacancy in ZnO to be at or below the midgap, using GW approximation calculations.[14]

The above examples show that the macroscopic correlation between functionality and oxygen supply during growth seems to evoke a lot of interesting phenomena. However, much less is known about the local atomic structure of the functional oxides on the availability of oxygen. To contribute to this question, we

Institut für Experimentelle Physik II, Universität Leipzig, Linnéstr. 5, 04103 Leipzig, Germany. E-mail: mlorenz@physik.uni-leipzig.de

† Present address: Steinstr. 23, D-04275 Leipzig, Germany.

This journal is © The Royal Society of Chemistry 2014

J. Mater. Chem. C, 2014, **2**, 4947–4956 | 4947

use as a model system, Mn^{2+} ions as paramagnetic probes in heteroepitaxial ZnO. The ZnO : Mn thin films are grown by PLD on a-plane sapphire substrates in a wide range of oxygen partial pressures. Electron paramagnetic resonance (EPR) spectroscopy of the Mn^{2+} ions allows monitoring the influence of the oxygen growth pressure on the structural properties of the films on a local scale by precise measurements of the zero field splitting (ZFS) of the divalent manganese ions. The Mn^{2+} ZFS parameters are then correlated with (volume-averaged) in-plane and out-of-plane lattice constants a and c of the thin films, respectively, as obtained by high-resolution X-ray diffraction (HR-XRD).

2. Electron paramagnetic resonance of Mn^{2+} in ZnO thin films

The incorporation site and the electronic state of paramagnetic transition metal ions in ZnO bulk materials have extensively been studied by EPR spectroscopy.[15,16] Divalent ions such as Mn^{2+} are incorporated in the trigonally distorted tetrahedral Zn lattice sites (C_{3v} symmetry). Therefore, the Mn^{2+} EPR spectrum in ZnO displays a characteristic ZFS with an axial ZFS parameter $D = -707$ MHz as observed for weakly Mn-doped ZnO single crystals.[17,18] The D parameter is considered as a measure of the trigonal distortion of the oxygen tetrahedra by the Mn^{2+} ions substituting Zn^{2+} at the metal ion sites in the ZnO wurtzite structure. Indeed, a linear correlation $D \propto \varepsilon_V$ between D and the volume compression ratio of the unit cell

$$\varepsilon_V = \frac{a^2 c - a_0^2 c_0}{a_0^2 c_0} \tag{1}$$

was proposed for manganese doped ZnO thin films grown on c-plane sapphire substrates recently.[19] Here a_0 and c_0 are the lattice parameters of the undoped ZnO single crystals. Diaconu et al. state that while in single crystals both lattice axes a and c increase with increasing Mn content only the c-axis increases with increasing Mn content in thin films. Obviously, in such a case with a constant in-plane lattice parameter a, the ZFS parameter D will become proportional to the axial compression ratio $\varepsilon_c = c/c_0 - 1$. In that work the lattice parameters of the thin films were changed by different Mn^{2+} doping concentrations in the range 0.1 at% to 9.1 at% whereas other growth parameters were kept unchanged.[19] However, except for the lowest manganese concentration the complete 30 lines Mn^{2+} EPR spectrum could not be resolved in the spectra due to dipolar spectral broadening leading to appreciable errors in the estimated D parameters and preventing further the analysis of the distribution widths of the ZFS parameters. The latter may give additional local information about strain effects in the thin films.

Therefore, in the present work we choose only low manganese concentrations of either 0.2 or 0.02 at% to avoid dipolar line broadening and to access the full spectral information of the Mn^{2+} EPR spectra. Moreover, the low doping levels prevent a significant increase in the c-axis lattice parameter of the films that might already be caused by the direct Mn^{2+} incorporation in the Zn sites of ZnO films.[19,20] In that way, we are now able to measure precisely both c-plane and a-plane lattice parameters of the ZnO thin films and the Mn^{2+} ZFS parameters and their distribution widths that are dependent on the oxygen partial pressure during their PLD growth process without the interference of other crucial parameters. The ZFS parameters are correlated with the c- and a-lattice constants of the films and the displacement of the Mn^{2+} in the oxygen tetrahedra along the c-axis using the superposition model.

3. Results

3.1. Structural characterization

Fig. 1 shows typical results of the structural investigations by XRD and HR-XRD. All ZnO films grow with perfect c-axis orientation on a-plane sapphire (Fig. 1a) and c-plane ZnO, in agreement with previous investigations.[21] The HR-XRD rocking curves and reciprocal space maps (RSMs) show remarkable differences for hetero- and homoepitaxial samples, for numerical values of the FWHM of the ZnO(002) rocking curves see Table 1. Fig. 1b shows three typical ZnO(002) rocking curves with FWHM from 0.0129° to 0.320°, indicating huge differences in tilt mosaicity of the sample types. The different structural quality of hetero- and homoepitaxial ZnO is further explained by the RSMs in Fig. 1c–f. Here, in addition to the tilt mosaicity expressed by the horizontal broadening of (002) reflections, the broadening of skew-symmetric (101) reciprocal lattice points demonstrates the twist mosaicity, because these peaks are measured with a high chi-tilt angle of 61.61° in HR-XRD. In contradiction to the clearly higher tilt and twist mosaicity of the heteroepitaxial films, the uncertainty of d-spacing as expressed by the vertical broadening of the reciprocal lattice points, is much lower. The extrapolated out-of plane and in-plane lattice constants of all samples are listed in Table 1.

Fig. 2 shows the oxygen partial pressure dependence of the c- and a-axis lattice parameters and the FWHM of the ZnO(002) rocking curves. The lattice parameters of all samples show an almost smooth variation with the oxygen partial pressure, indicating c-axis expansion and a-axis compression of ZnO with decreasing oxygen pressure, i.e. increasing concentration of oxygen vacancies (Fig. 2a and b).[22] This in-plane contraction and out-of-plane expansion of the c-axis oriented ZnO unit cells are in qualitative agreement with calculated local atomic relaxations around the neutral oxygen vacancy V_O^0, see Fig. 4 in ref. 23, as obtained from first-principle local density approximations.

For the FWHM (002), three samples were intentionally included which do not follow the general behavior of the majority of films, probably because of substrate issues (top right in Fig. 2c). However, all samples from Fig. 2c fit well the results discussed further below, demonstrating the general validity of our work.

3.2. EPR spectroscopy

The EPR spectra of the heteroepitaxial ZnO : Mn thin films (Fig. 3 and 4) and of the homoepitaxial ZnO : Mn films (Fig. 5a) display the typical thirty line spectrum of Mn^{2+} ions with their $3d^5$ electronic configuration having a $^6S_{5/2}$ electronic ground state for the two orientations of the external magnetic field,
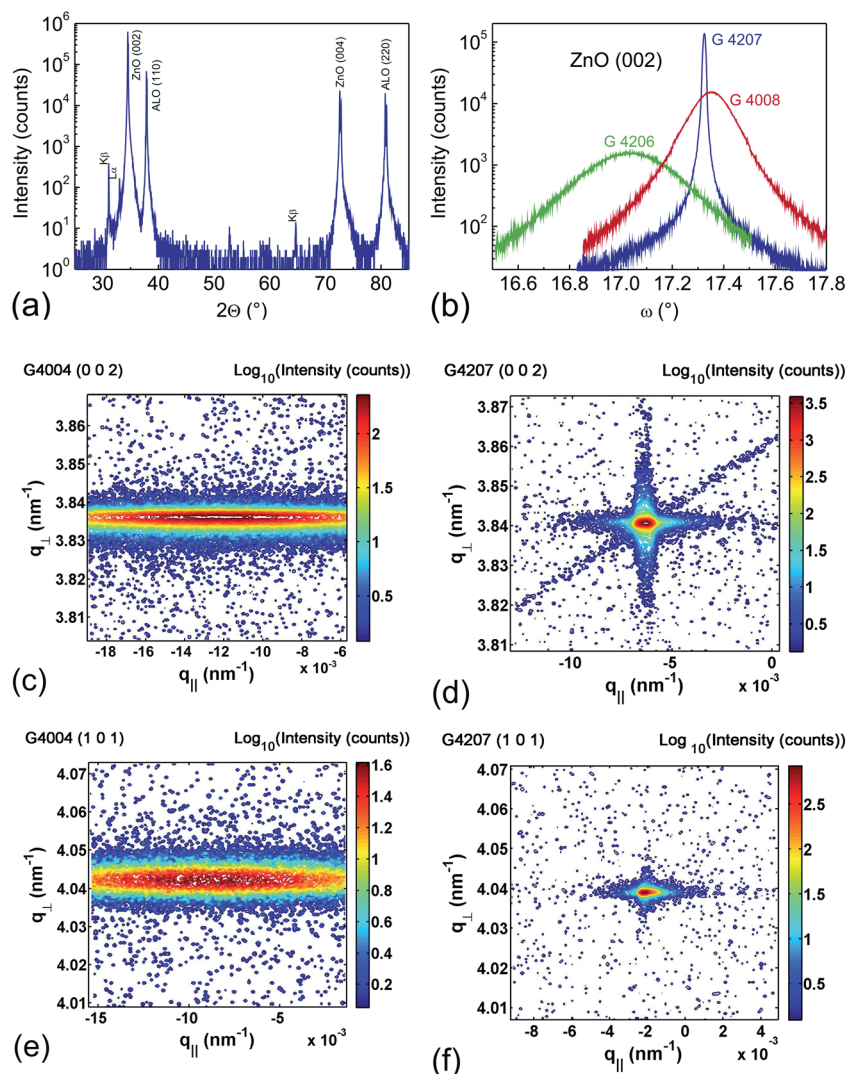
4948 | J. Mater. Chem. C, 2014, 2, 4947–4956

This journal is © The Royal Society of Chemistry 2014

Fig. 1 Typical XRD results of the hetero- and homoepitaxial ZnO : Mn films: (a) wide-angle $2\theta - \omega$ scan shows only ZnO(002), (004) and Al$_2$O$_3$(110), (220) peaks. (b) shows typical rocking curves of the ZnO(002) peak as a measure of tilt mosaicity. For the homoepitaxial sample G4207, ZnO : Mn film and ZnO substrate peaks cannot be separated. (c) and (e) are ZnO(002) and (101) reciprocal space maps (RSMs) of the heteroepitaxial sample G4004, respectively, while (e) and (f) are the corresponding RSMs for the homoepitaxial sample. Obvious are the differences in horizontal and vertical broadening of the reciprocal lattice points, accounting for tilt (002) and twist (101) mosaicity, and d-spacing blurring, respectively.

parallel or perpendicular to the crystallographic c-axis. Here the total electron spin $S = 5/2$ gives rise to a zero field splitting into five fine structure (fs) transitions, each split into six hyperfine (HF) interaction lines due to the HF interaction with the nuclear spins $I = 5/2$ of the ^{55}Mn nuclei. If we assume isotropic electron Zeeman and ^{55}Mn HF interactions the EPR spectra of the Mn^{2+} ions can be described by the following spin Hamiltonian,[17,18,24]

$$\hat{H} = \beta \vec{B} g \hat{\vec{S}} + D\left[\hat{S}_z^2 - \frac{35}{12}\right] + E\left[\hat{S}_x^2 - \hat{S}_y^2\right]$$

$$+ \frac{a}{6}\left[\hat{S}_\xi^4 + \hat{S}_\eta^4 + \hat{S}_\zeta^4 + \frac{707}{16}\right]$$

$$+ \frac{7F}{36}\left[\hat{S}_z^4 - \frac{95}{14}\hat{S}_z^2 + \frac{81}{16}\right] + \hat{\vec{S}} A \hat{\vec{I}} \qquad (2)$$

where g is the electron g-factor and A the ^{55}Mn HF interaction parameter. The ^{55}Mn nuclear quadrupole interaction has been neglected in eqn (2) as it has no effect on the allowed EPR transitions in the spectra recorded for $\vec{B} \parallel c$ and $\vec{B} \perp c$ that have been analyzed here. D refers to the axial ZFS and a and F are the cubic ZFS parameters. The (x, y, z) and (ξ, η, ζ) coordinates refer to the trigonal and cubic axes of the crystal field, respectively. Although the Mn^{2+} ions are incorporated in nominally axially symmetric Zn^{2+} lattice sites (C_{3v} symmetry) a rhombic contribution to ZFS measured by the parameter E has been included in the spin Hamiltonian. It may allow for possible rhombic distortions of the crystal field in the heteroepitaxial ZnO : Mn films acting on the manganese ions due to strains caused by the sapphire substrate.

This journal is © The Royal Society of Chemistry 2014

J. Mater. Chem. C, 2014, **2**, 4947–4956 | **4949**

Table 1 Oxygen partial pressures p_{O_2} during PLD, manganese concentrations in the PLD target c_{MnO}, extrapolated HR-XRD c- and a-axis lattice parameters, FWHM of the ZnO(002) rocking curve, and ZFS parameter D with ZFS distribution widths ΔD and ΔE, of the ZnO : Mn thin films on a-plane sapphire. Sample G4207 was homoepitaxially grown on c-plane ZnO (O-face)

Sample	p_{O_2} (mbar)	c_{MnO} (%)	c (Å)	a (Å)	FWHM (°)	D (MHz)	ΔD (MHz)	ΔE (MHz)
G4438	6×10^{-5}	2×10^{-2}	5.2305	3.242	0.452	—	—	—
G4437	3×10^{-4}	2×10^{-2}	5.2267	3.246	0.357	−584	140	40
G4009	2×10^{-3}	2×10^{-2}	5.2233	3.249	0.195	−611	110	40
G4005	2×10^{-3}	2×10^{-1}	5.228	3.245	0.225	−611	100	40
G4592	5×10^{-3}	2×10^{-2}	5.2263	3.246	0.160	−606	95	20
G4207^a ZnO substrate	1.6×10^{-2}	2×10^{-2}	5.2063	3.2497	0.0129	−707	10	0
G4008	1.6×10^{-2}	2×10^{-2}	5.2131	3.247	0.148	−650	35	15
G4004	1.6×10^{-2}	2×10^{-1}	5.2130	3.246	0.130	−653	40	20
G4591	5×10^{-2}	2×10^{-2}	5.2085	3.249	0.134	−674	35	15
G4436	8×10^{-2}	2×10^{-2}	5.2065	3.249	0.568	−703	180	40
G4206	1.6×10^{-1}	2×10^{-2}	5.2061	3.250	0.320	−707	120	40
G4590	5×10^{-1}	2×10^{-2}	5.2084	3.2475	0.194	−671	90	20

^{a} For Mn^{2+} in the ZnO single crystalline substrate, which, however, also contains Fe, Co, Ni. Assuming a homogeneous Fe distribution in the film and the substrate, $c_{Fe(III)}$ is 2.3×10^{15} ions per sample.
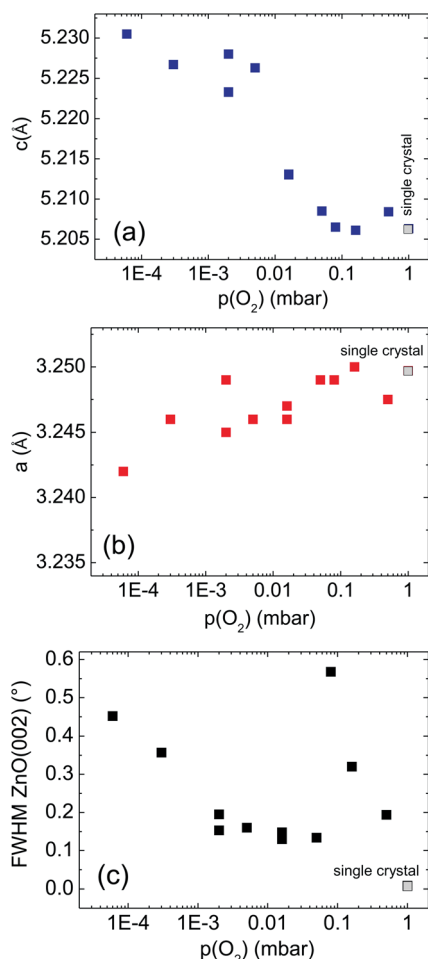
Fig. 2 Oxygen partial pressure dependence of (a) out-of-plane c-axis lattice parameter, (b) in-plane a-axis lattice parameter, and (c) FWHM of the ZnO(002) rocking curves. Data of the homoepitaxial sample (the ZnO single crystal) are marked by the gray filled symbols.
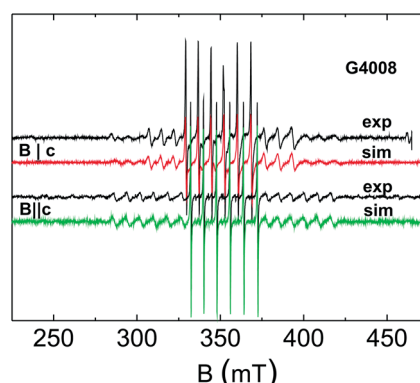
Fig. 3 Experimental and simulated EPR spectra at 297 K of the ZnO : 0.02% Mn ($p_{O_2} = 1.6 \times 10^{-2}$ mbar) thin film sample G4008 for $\vec{B}||$ c and $\vec{B} \perp c$.
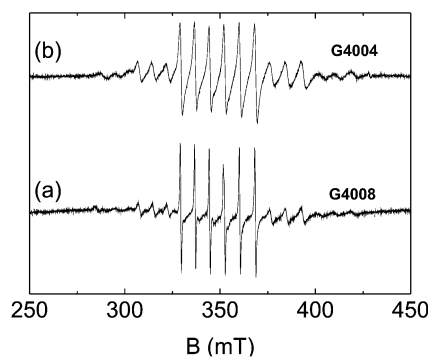
Fig. 4 Experimental EPR spectra at 297 K of (a) ZnO : 0.02% Mn (G4008) and (b) ZnO : 0.2% Mn (G4004) thin films both grown at $p_{O_2} = 1.6 \times 10^{-2}$ mbar $\vec{B} \perp c$.

As a typical example for a heteroepitaxial ZnO : Mn film Fig. 3 illustrates the experimental Mn^{2+} EPR spectra of the ZnO:0.02% Mn ($p_{O_2} = 1.6 \times 10^{-2}$ mbar) thin film sample G4008
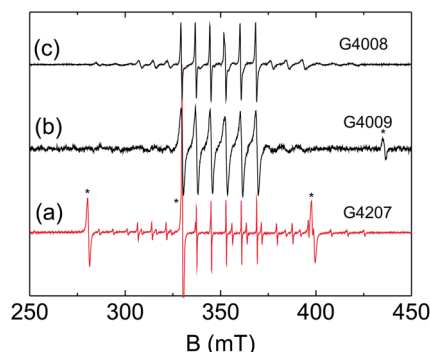
Fig. 5 Experimental single crystal EPR spectrum (sample G4207) (a) and EPR spectra of ZnO : 0.02% Mn thin film samples grown under oxygen partial pressures of (b) $p_{O_2} = 1.6 \times 10^{-3}$ mbar (G4009) and (c) $p_{O_2} = 1.6 \times 10^{-2}$ mbar (G4008). The spectra were recorded at 297 K for $\vec{B} \perp c$. Asterisks indicate signals of Fe^{3+} impurities in either the sapphire substrate (films) or the ZnO single crystal G4207.

for $\vec{B} \parallel c$ and $\vec{B} \perp c$ together with simulated spectra based on the spin Hamiltonian in (2). The line widths of the five fs transitions centered at 265 mT ($m_S = 5/2 \leftrightarrow 3/2$), 306 mT ($m_S = 3/2 \leftrightarrow 1/2$), 351 mT ($m_S = 1/2 \leftrightarrow -1/2$), 396 mT ($m_S = -1/2 \leftrightarrow -3/2$), and 441 mT ($m_S = -3/2 \leftrightarrow -5/2$) for $\vec{B} \parallel c$ differ significantly and increase with increase in the magnetic spin quantum number m_S. Such a behavior is indicative of a distribution in the ZFS parameters and has been taken into account by Gaussian distributions of the ZFS parameters D and E with the corresponding distribution widths ΔD and ΔE in our spectral simulations. We have to note that the spectra for $\vec{B} \parallel c$ are only influenced by the axial ZFS parameter D in the case of isotropic g-tensors whereas the spectra are sensitive to both, D and E, for $\vec{B} \perp c$. Therefore, the distributions ΔD and ΔE can be separated from each other by simulations of spectra recorded for the two different orientations.

The simulations revealed an axial ZFS parameter $D = -650$ MHz with distribution width $\Delta D = 35$ MHz and a small distribution $\Delta E = 15$ MHz of the rhombic ZFS parameter about $E = 0$ (Table 1). The D parameter is in the typical range reported for Mn^{2+} incorporated in Zn^{2+} lattice sites in ZnO.[17–19] The overall axial symmetry of the ZFS interaction ($E = 0$) was confirmed by a rotation of the magnetic field perpendicular to the c-axis of the film where no significant changes of the positions or line widths of the four outer fs transitions ($m_S = \pm 3/2 \leftrightarrow \pm 1/2$, $m_S = \pm 5/2 \leftrightarrow \pm 3/2$) have been observed for sample G4008. In the simulations an isotropic g-value $g = 2.001$ and an isotropic ^{55}Mn HF interaction parameter $A = -222$ MHz was assumed. The negative sign of the D parameter can be deduced from the spectral simulations. In particular the field positions of the $m_S = \pm 3/2 \leftrightarrow \pm 1/2$ transitions depend on the sign of the parameter ratio A/D. The cubic ZFS parameters $a = 18$ MHz and $F = 12$ MHz were taken from a single crystal study of Mn^{2+} ions in ZnO.

The influence of the Mn^{2+} concentration on the ZFS parameters has been examined at two distinct oxygen partial pressures, $p_{O_2} = 1.6 \times 10^{-2}$ mbar (samples G4008 and G4004) and $p_{O_2} = 2 \times 10^{-3}$ mbar (samples G4009 and G4005), during the PLD process. Although the Mn^{2+} concentrations differ in

each case by one order of magnitude the ZFS parameters D and E as well as their distribution widths ΔD and ΔE as determined by spectral simulations do not vary significantly (Table 1). However, the higher Mn^{2+} doping results in a substantial increase in the homogeneous EPR line widths ΔB_{pp}^{hom} as seen in Fig. 4 for the samples G4008 and G4004 due to enhanced dipolar interactions between the paramagnetic ions in the higher doped films. Here ΔB_{pp}^{hom} increases from 9 MHz to 18 MHz with increasing Mn concentration whereas for samples G4009 and G4005 ΔB_{pp}^{hom} increases even by a factor of 3 (12 MHz versus 36 MHz).

In contrast to the concentration of the dopants the oxygen partial pressure p_{O_2} during the PLD process affects crucially the axial ZFS parameters D and ΔD. Fig. 5 illustrates the influence of p_{O_2} on the Mn^{2+} EPR spectra at $\vec{B} \perp c$ for two selected samples. Obviously, the line widths caused by the distribution in the ZFS parameters increase strongly for the film prepared at lower oxygen partial pressures (Fig. 4b) leading to less resolved outer fs transitions. The spectral simulation for both film orientations $\vec{B} \perp c$ and $\vec{B} \parallel c$ (spectra not shown) indicates clearly that this increase in line broadening is mainly caused by the distribution ΔD in the axial ZFS parameter D. There is also an effect of the oxygen partial pressures on the distribution ΔE of the rhombic fs parameter E but it appears to be less pronounced. In addition to the ΔD values, the absolute value of the axial ZFS parameter D depends likewise in a characteristic manner on p_{O_2}. Overall it decreases with lower oxygen partial pressures. All ZFS parameters of the studied films as obtained from the spectral simulations are summarized in Table 1. In addition the ZFS parameters of Mn^{2+} impurities present in the homoepitaxial ZnO : Mn film sample (G4207) are presented in the table as well. For comparison its EPR spectrum is also displayed in Fig. 5a. It is worth noting that the ΔD parameter in the homoepitaxial ZnO : Mn film sample is substantially smaller (by a factor of four or more) than those of the heteroepitaxial film samples. In the case of the homoepitaxial sample we have to take into account that Mn^{2+} and Fe^{3+} ions are also present in the ZnO single crystal substrate as impurities for EPR spectroscopy appreciable concentrations, compare ref. 25. In contrast the sapphire substrates did not exhibit EPR signals from Mn^{2+} impurities. Only some minor Fe^{3+} signals were detected in the measured magnetic field range that did not interfere with the Mn^{2+} spectrum of the ZnO : Mn films. But the EPR spectra of the homoepitaxial sample do not allow us to distinguish between manganese ions incorporated in the thin film and the Mn^{2+} impurities of the ZnO substrate since only a single Mn^{2+} species is observed. Moreover, as the Mn^{2+} signal intensity for the sample G4207 is substantially higher than those for the heteroepitaxial ZnO : Mn films we assume that the Mn^{2+} EPR signal of the homoepitaxial ZnO : Mn film is mainly caused by manganese impurity ions in the ZnO single crystal substrate. Indeed the obtained spin Hamiltonian parameters of its Mn^{2+} ions (Table 1) are in agreement with those reported for Mn^{2+} impurities in low concentrations in ZnO single crystals.[17,18] Therefore we may refer to this sample as a ZnO single crystal in the following and consider it as a reference sample for Mn^{2+} substitution in undisturbed ZnO single crystals.

This journal is © The Royal Society of Chemistry 2014

J. Mater. Chem. C, 2014, **2**, 4947–4956 | 4951

4. Discussion

The XRD data reveal an obvious relationship between the lattice axes parameters c and a and the oxygen partial pressure during the growth process. We suppose that the major reason for the observed dependence of this biaxial strain on p_{O_2} is the formation of oxygen vacancies at low p_{O_2} values. Pseudomorphic, *i.e.* in-plane lattice matched growth can be excluded for the heteroepitaxial ZnO films on sapphire. For films grown at $p_{O_2} > 5 \times 10^{-2}$ mbar both lattice constants appear to be comparable to the single crystal values. However, the c-axis parameter increases strongly with decreasing pressure for pressures $p_{O_2} < 5 \times 10^{-2}$ mbar, whereas the parameter a declines slightly. These opposing trends for c and a indicate that the volume of the unit cell of the ZnO films does not significantly change with oxygen partial pressure and stays comparable with that of the single crystal. This fact is illustrated by a comparison of the volume compression ratios ε_V for the various films with the single crystal value as displayed in Fig. 6.

The figure also includes the compression ratios for the c- and a-axes lattice parameters $\varepsilon_c = c/c_0 - 1$ and $\varepsilon_a = a/a_0 - 1$. The data suggest that the unit cell of the ZnO films shrink perpendicular to the crystallographic c-axis with increasing formation of oxygen vacancies at lower oxygen partial pressures and consequently the bond length between the Zn^{2+} ion and the three non-axial oxygen atoms in the ZnO_4 tetrahedra are becoming shorter. This, however, is related to an increase in the axial Zn–O bond length $R_1(0)$ along the c-axis as the overall unit cell volume is conserved. For lower oxygen partial pressures and enhanced oxygen vacancy formation the strain in the films seems to increase as well as indicated by the widths of the diffraction peaks (Fig. 1c).

Supplementary to the XRD data the manganese ZFS parameters as determined from EPR spectroscopy provide a microscopic perspective at the changes of the ZnO_4 or more precisely the MnO_4 tetrahedra upon the enhanced formation of oxygen vacancies with decreasing oxygen partial pressures in the ZnO films. Indeed, we observe within the experimental accuracy almost linear correlations between the axial ZFS parameter D and the axis lattice parameter ratio c/a of the films and between distribution widths ΔD of the axial ZFS parameter and the

widths of the diffraction peaks (Fig. 7). In that way a correlation can be established between the c/a ratio and the distortions of the metal ion–oxygen tetrahedra. The results confirm that the MnO_4 tetrahedra experience the same structural modification as the ZnO_4 units and the paramagnetic Mn^{2+} ions can be considered to be suitable probes to monitor the structural variations of the films on a local microscopic scale. However, the D parameter of the Mn^{2+} ions would not become zero even for an assumed case of an ideal wurtzite structure[22] ($c/a = (8/3)^{1/2}$), see Fig. 7a. The reason is a small displacement δ of the Mn^{2+} ions with respect to the Zn^{2+} site along the c-axis in the metal–oxygen tetrahedron presumably due to minor differences in the ionic radii.[24,26] We have to note that the axial ZFS parameter D monitors the increase of the axial metal ion–oxygen bond length R_1 along the c-axis, which is related to an axial elongation of the unit cell and an increase in the lattice parameter c as observed in the XRD experiments. In addition, the determined distribution widths ΔD of the axial ZFS parameter point at some variance in the bond lengths R_1 and consequently at some structural distortions of the MnO_4 tetrahedra depending on oxygen growth pressure and the formation of oxygen vacancies in the films. Moreover, a small distribution ΔE of the rhombic ZFS parameter about $E = 0$ was likewise observed for all studied ZnO thin films (Table 1) indicating some deviation from the perfect C_{3v} symmetry of the tetrahedra. This might be caused either by slightly different non-axial metal ion–oxygen bond
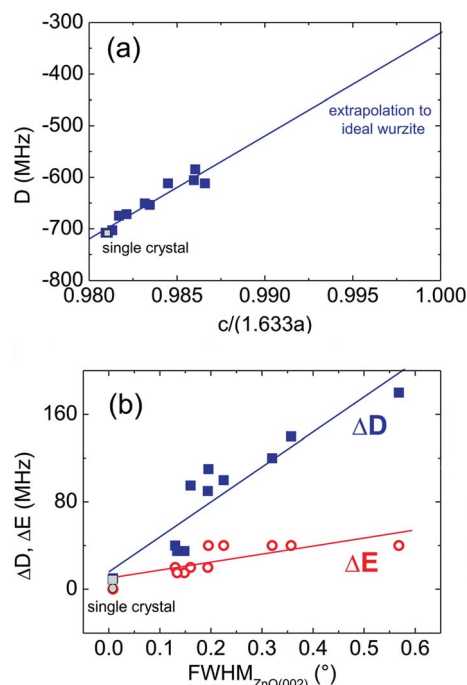
Fig. 7 Experimentally determined (a) ZFS parameter D depending on the ratio of the lattice parameters c and a and (b) ZFS distribution widths (filled squares) ΔD and (open circles) ΔE depending on FWHM of the ZnO(002) peak for ZnO thin film samples and the ZnO single crystal (gray filled symbols). The scaling $1.633 = (8/3)^{1/2}$ in the c by a ratio takes into account the lattice parameter ratio $c/a = (8/3)^{1/2}$ of the ideal wurtzite structure.[22] The solid lines are linear fits to the data points.
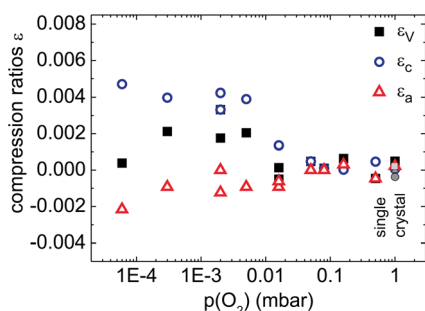

Fig. 6 Volume compression ratio ε_V (solid squares) and axes compression ratios ε_a (open triangles) and ε_c (open circles) of the ZnO single crystal and ZnO thin film samples depending on oxygen partial pressures p_{O_2}. Gray filled symbols indicate single crystal data.

lengths or bond angles. Otherwise for the ZnO single crystal the EPR spectra reveal $\Delta E = 0$ within the experimental accuracy. Therefore we suppose that the distortions of the C_{3v} symmetry of the tetrahedra indicate the presence of small strains in the films due to a misfit between the ZnO films and the a-sapphire substrates.

In the final step we want to rationalize why the absolute value of the ZFS parameter D decreases with increasing axial elongation of the metal ion–oxygen tetrahedra as indicated by the increase of the axis parameter c with decreasing p_{O_2} (Fig. 7a). Our analysis will further provide an interpretation of the experimentally obtained D parameters of the Mn^{2+} ions in terms of displacements of the metal ion in the oxygen tetrahedra depending on the axes lattice parameters c and a of the ZnO films.

Recently, Zi-Yuan[26] derived a local structure model of the MnO_4 tetrahedra from the D parameter of Mn^{2+} ions measured for lightly doped ZnO single crystals ($D = -707$ MHz) using the superposition model.[27] In the proposed model the structures of the MnO_4 tetrahedra differ slightly from those of the ZnO_4 tetrahedra in the parent ZnO material. The Mn^{2+} ion is displaced by $\delta = 0.03$ Å with respect to the Zn^{2+} site along the c-axis towards the basal of the oxygen tetrahedra. Here, the displacement $\delta = 0.03$ Å was taken from the average ionic radii of Mn^{2+} (0.8 Å) and Zn^{2+} (0.74 Å). Then, the D value was assumed to be related to a small deviation $\Delta\theta = 1°$ of the angle θ between c-axis and the bond directions of the three non-axial basal oxygen ions in the MnO_4 tetrahedra in comparison with the parent ZnO_4 tetrahedra. However, as only a single experimental D value with a single set of structural data, those from the single crystal, was used the validity of the structure model could not be tested.

By exploring the Mn doped ZnO thin films grown under different oxygen partial pressures we have a whole set of ZnO materials with different structural parameters and corresponding Mn^{2+} D ZFS parameters available to identify the structure of the MnO_4 tetrahedra. In order to interpret the axial ZFS parameters we use high-order perturbation theory based on the spin–orbit coupling mechanism for S-state ions in a weak-field scheme[28,29] for the computation of the dependence of D on the structural parameters of the ZnO thin films. We postulate likewise that the Mn^{2+} ions are incorporated in the Zn^{2+} lattice sites but may be displaced by δ with respect to the zinc site along the c-axis towards the basal of the oxygen tetrahedra (Fig. 8) due to the slightly larger

ionic radii of Mn^{2+} *versus* Zn^{2+}. However, we do not assume a fixed displacement but rather consider δ as a function of the lattice parameters c and a that depend on the oxygen partial pressure during the growth process.

The axial ZFS parameter D that depend on the crystal field parameters B_{20}, B_{40}, and B_{43} in the case of trigonal symmetry has been calculated in the weak field scheme, where the total crystal field and the spin–orbit coupling are taken as perturbations, by Ju *et al.*[28] and Zheng *et al.*[29]

$$D \approx -P_1(B,C)^{-1}(3\xi_d^2 B_{20}^2 + 63\xi_d^2 B_{20}) \\ - P_2(B,C)^{-1}(10\xi_d^2 B_{40}^2 - 7\xi_d^2 B_{43}^2). \tag{3}$$

The parameters

$$P_1(B,C) = 70(7B + 7C)^2(17B + 5C) \tag{4}$$

and

$$P_2(B,C) = 126(7B + 7C)^2(10B + 5C) \tag{5}$$

are solely determined by the Racah parameters $B = 960$ cm^{-1} and $C = 3352$ cm^{-1}.[26] $\xi_d = 308$ cm^{-1} is the spin–orbit coupling constant of the Mn^{2+} ions. The dependencies of the crystal field parameters B_{20}, B_{40}, and B_{43} on the bond lengths R_1 and R_2 between the Mn^{2+} ion and the axial and basal oxygen next neighbors (Fig. 8) are calculated using the approximation of the superposition model[27]

$$B_{20} \approx A_2\left[2\left(\frac{R_0}{R_1}\right)^{t_2} + 3\left(3\cos^2\theta - 1\right)\left(\frac{R_0}{R_2}\right)^{t_2}\right] \tag{6}$$

$$B_{40} \approx A_4\left[8\left(\frac{R_0}{R_1}\right)^{t_4} + 3\left(35\cos^4\theta - 30\cos^2\theta + 3\right)\left(\frac{R_0}{R_2}\right)^{t_4}\right] \tag{7}$$

and

$$B_{43} \approx -6\sqrt{35}A_4\sin^3\theta\cos\theta\left(\frac{R_0}{R_2}\right)^{t_4} \tag{8}$$

with the reference distance $R_0 = 1.9813$ Å, the exponents $t_2 = 3$ and $t_4 = 5$ and the two parameters $A_4 = -27\ Dq/16$ and $A_2 = 12\ A_4$, where $Dq = -650$ cm^{-1} is the cubic crystal field splitting parameter.[26] The bond distances R_1 and R_2 as well as the angle θ between directions of bonds between the manganese ion with the basal and axial oxygen ions depend on the displacement δ (Fig. 8) and are given by

$$R_1(\delta) = uc - \delta \tag{9}$$

$$R_2(\delta) = \sqrt{a^2/3 + (c(u - 1/2) - \delta)^2}, \tag{10}$$

$$\theta(\delta) = \arccos\frac{c(u - 1/2) - \delta}{R_2(\delta)}, \tag{11}$$

with the parameter $u = 0.3819$ for ZnO.[30] Here, $\delta > 0$ corresponds to displacements of the Mn^{2+} ions towards the axial oxygen ion with respect to the Zn^{2+} site whereas negative values of δ indicate a relative shift of the substitutional ion towards the basal oxygen ions.
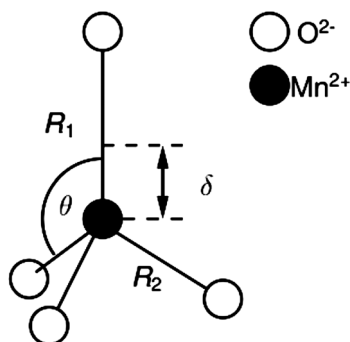

Fig. 8 Schematic drawing of the structure of the MnO_4 tetrahedra in the ZnO : Mn films with the structural parameters θ, R_1, R_2, and δ.
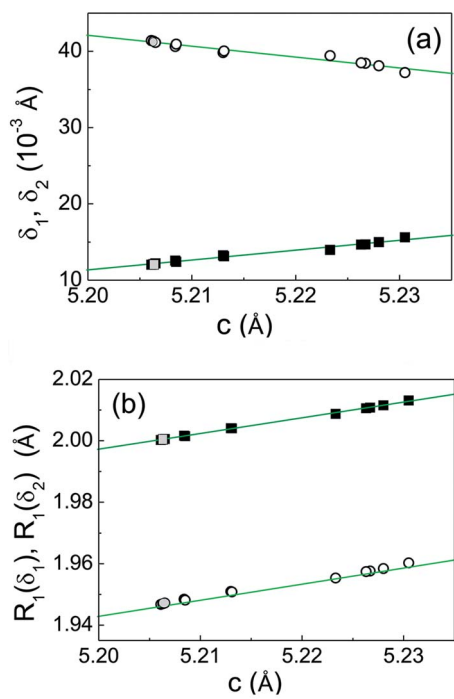
This journal is © The Royal Society of Chemistry 2014

J. Mater. Chem. C, 2014, **2**, 4947–4956 | **4953**

Fig. 9 (a) Absolute values of calculated displacements (solid squares) δ_1 and (open circles) δ_2 of the Mn^{2+} ions along the c-axis in the MnO_4 tetrahedra and (b) corresponding bond lengths R_1 (solid squares for solutions δ_1, open circles for solutions δ_2) between the Mn^{2+} ions and the axial oxygen ion depending on the c-axis crystal parameter as obtained for ZnO thin film samples and the ZnO single crystal (gray filled symbols).
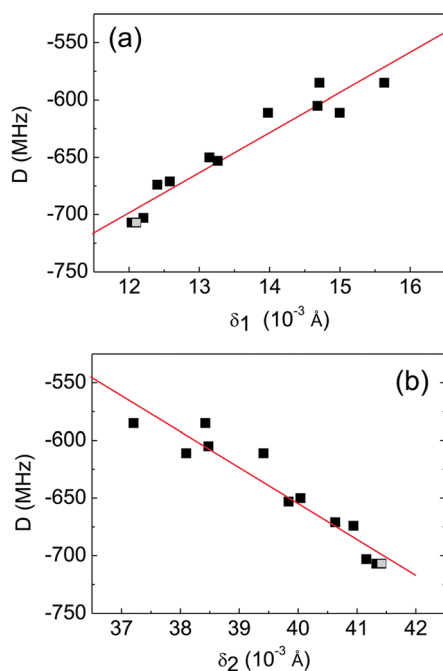

Fig. 10 Correlation between experimentally determined axial ZFS parameter D and absolute values of displacements (a) δ_1 and (b) δ_2 of the Mn^{2+} ions along the c-axis in the MnO_4 tetrahedra as obtained for ZnO thin film samples and the ZnO single crystal (gray filled squares).

The displacement δ of the Mn^{2+} ion along the c-axis with respect to the positions of the Zn^{2+} site can then be determined numerically for each set of film parameters c, a, and D by solving eqn (3)–(11). Two solutions $\delta_1 < 0$ and $\delta_2 > 0$ for the displacements are obtained for each parameter set and their absolute values are displayed to be dependent on the c-axis lattice parameter in Fig. 9a. The corresponding bond angles for the two solutions $\theta_1 = 107.7°$ and $\theta_1 = 109.5°$ vary by only $\pm 0.1°$ within the obtained range of $\delta_{1,2}$ values. Using eqn (9) two choices for the bond length between the Mn^{2+} ion and the axial oxygen ion, $R_1(\delta_1)$ and $R_1(\delta_2)$, can be calculated for the two solutions δ_1 and δ_2 (Fig. 9b).

In the case of $R_1(\delta_1)$ the Mn^{2+} ion is displaced towards the axial oxygen ion along the c-axis with respect to the Zn^{2+} site whereas for $R_1(\delta_2)$ it is shifted towards the basal oxygen ions of the tetrahedron. In each situation the Mn–O bond distances increase with the increasing lattice axis parameter c and enhanced formation of oxygen vacancies with decreasing p_{O_2} during the growth of the ZnO films. The crystal field at the manganese ion becomes weaker with the increasing c-axis parameter. This explains why the absolute value of the axial ZFS parameter D decreases with increasing lattice axis parameter c although the axial distortion of the tetrahedron becomes larger. Fig. 10 illustrates the linear dependence of D on the absolute values of the computed displacement solutions δ_1 and δ_2.

On the basis of our analysis of the D parameter we cannot safely rule out one of the two possible Mn^{2+} positions described by $R_1(\delta_1)$ and $R_1(\delta_2)$. We may only speculate that a displacement $R_1(\delta_1)$ towards the axial oxygen ion with respect to the Zn^{2+} position seems to be more likely as that such a shift has been observed for divalent manganese ions incorporated in the likewise axially distorted tetrahedral metal sites in GaN and AlN.[17,18,24] However, we can firmly rule out the above discussed model suggested by Zi-Yuan *et al.* where the axial ZFS splitting was assumed to be caused only by a variation in the angle θ between the MnO_4 and the host ZnO_4 tetrahedra.[26] Varying exclusively the angle θ in eqn (6)–(8) but keeping R_1 and R_2 constant, we have not been able to reproduce our experimental D parameters.

5. Experimental

ZnO : Mn thin films were grown by PLD using a KrF excimer laser from polycrystalline source targets mixed, pressed and sintered from ZnO and MnO powders (Alpha Aesar, 5N purity). As a substrate we used a-plane sapphire, or a c-plane O-face ZnO single crystal, both supplied by CrysTec GmbH. The growth temperature of the films was about 650 °C and 45 000 laser pulses were applied. The oxygen partial pressure was controlled in between 10^{-1} and 6×10^{-5} mbar. Table 1 gives an overview of the samples (for identification of consecutively grown samples we maintain the original sample ID no.). For more details of our ZnO thin film growth activities see ref. 21 and references therein.

XRD rocking curves and reciprocal space maps were measured with a Philips X'pert diffractometer with Cu $K_{\alpha1}$ point focus, a $4\times$ Ge (220) Bartels primary monochromator, a 4-axis goniometer (Eulerian craddle), and either an open detector or a secondary monochromator (triple axis), respectively. XRD

wide-angle $2\theta - \omega$ scans were measured with Cu K$_{\alpha 1/2}$ radiation and the focussing Bragg Brentano goniometer (Philips X'pert) with a graphite secondary monochromator for suppression of bremsstrahlung. For highly precise determination of out-of-plane (*c*) and in-plane (*a*) lattice constants of the heteroepitaxial films we used a PANalytical X'pert PRO MRD with a parabolic mirror and a Bartels monochromator as primary optics with Cu K$_{\alpha 1}$ line focus and the PIXcel^{3D} detector in 1D scanning mode with 255 channels. In order to precisely correct the goniometer height errors, we measured (002), (004), and if possible also (006) symmetric and (101) and (202) asymmetric peaks, and extrapolated the lattice constants from plots over $\cos^2(\theta)$. This method was recently proved to yield highly precise (5×10^{-4} and 5×10^{-5}) lattice constants for heteroepitaxial ZnO films and single crystals, respectively, in agreement with independently determined values from X-ray multiple reflections.[31]

Proton induced X-ray emission (PIXE) and Rutherford backscattering spectrometry (RBS) were used for determination of Mn concentration, layer thickness, and for trace element analysis. A 1.2 MeV H$^+$ beam of the Leipzig ion probe LIPSION with a beam diameter of 0.4 mm and a collected charge of 10 μC per measurement was used. PIXE and RBS spectra were fitted with the GeoPIXE II[32] and RUMP[33] software, respectively.

The obtained Mn concentrations confirmed within the experimental uncertainty that the PLD target compositions were transferred almost unchanged into the ZnO : Mn thin films. The metal to oxygen ratio was 1.00 ± 0.02 for the samples grown at intermediate oxygen partial pressure. The ZnO : Mn film thickness of the heteroepitaxial samples was determined to be between 1.08 and 1.46 μm, depending on the growth conditions and using a mass density of 5.62 g cm^{-2}. These thickness values are in good agreement with the HR-XRD result of the homoepitaxial sample G4207, where around ZnO(002) Pendellösung oscillations could be observed (see Fig. 1d). The mean fringe period of 0.00653° yields a mean ZnO : Mn thickness of 1.41 ± 0.10 μm for this particular sample.

EPR experiments have been performed on an X-band Bruker ELEXSYS E580 spectrometer at room temperature using a cylindrical ER4119 HS cavity. The ZnO thin film samples (area size 2 mm × 4 mm) and the ZnO single crystal (with homoepitaxial ZnO : Mn film) were mounted on a quartz rod sample holder. The angle between the *c*-axis of the ZnO crystal and the direction of the applied magnetic field was controlled by a goniometer. Spectral simulations of the Mn^{2+} EPR spectra were done using the EasySpin EPR simulation package[34] which employs full matrix diagonalization of the complete Mn^{2+} spin Hamiltonian operator.

6. Summary and conclusions

The influence of the oxygen partial pressure during the PLD growth process on the structural properties was explored for manganese doped heteroepitaxial ZnO thin films by HR-XRD and EPR spectroscopy of Mn^{2+} ions substituting Zn^{2+} in the ZnO lattice. This combined approach allowed us to correlate the induced changes of the overall film structure with the local properties at the tetrahedral incorporation site of the divalent

manganese ions. Our work reveals a significant expansion of the ZnO film structure along the *c*-axis combined with the *a*-axis compression with decreasing oxygen partial pressure that we ascribe to the enhanced formation of oxygen vacancies under oxygen deficient growth conditions. This increase of the *c*-axis lattice parameter translates into an increase of the bond distances between the metal ions and the axial oxygen ions along the *c*-axis in the metal ion–oxygen tetrahedra of the ZnO films. In the case of Mn^{2+} substituting Zn^{2+} this enlargement of the Mn–O bond distance is monitored by the axial Mn^{2+} ZFS parameter *D*. Using the superposition theory of crystal fields, the Mn–O bond distances could be calculated from the *D* parameter for the distinct oxygen partial pressures and related to the *c*-axis lattice parameters. In that way, linear relations have been obtained between the *c*-axis expansion and the ZFS parameter *D* as well as the axial Mn–O bond distance R_1. Although the *D* parameter decreases by about 120 MHz for the films grown under the lowest oxygen partial pressure ($p_{O_2} = 3 \times 10^{-4}$ mbar) used here in comparison with films grown at $p_{O_2} = 1.6 \times 10^{-1}$ mbar or the ZnO single crystal, the corresponding increase in the axial Mn–O bond distance R_1 is only 0.013 Å that indicates the high sensitivity of the Mn^{2+} ZFS parameter with respect to small local structural distortions. We assume that the Mn^{2+} ion is slightly shifted towards the axial oxygen ion with respect to the Zn^{2+} site. In this case, the bond distance between the Mn^{2+} ion and the axial oxygen ion will increase with the increasing *c*-axis lattice parameter in comparison with the corresponding axial Zn–O bond length and the displacement of the Mn^{2+} ion from the Zn^{2+} site becomes smaller with an enhanced expansion of the ZnO lattice.

We would like to emphasize that the enhanced formation of oxygen vacancies at lower oxygen partial pressures also results in higher structural distortions of the films as indicated by the increase of the width of the HR-XRD rocking curves and, locally measured by the EPR of the Mn^{2+} ions, the larger distribution widths of the ZFS parameter *D*. The latter could again be interpreted in terms of increasing variation in the axial Mn–O bond distance R_1 at higher oxygen vacancy concentrations. The presented investigations may be extended to doped oxide thin films with low Mn^{2+} concentration as local probes for lattice distortions and bond lengths.

Acknowledgements

References

1 S. X. Zhang, S. Dhar, W. Yu, H. Xu, S. B. Ogale and T. Venkatesan, *Appl. Phys. Lett.*, 2007, **91**, 112113.
2 M. Lorenz and R. Rao, *J. Phys. D: Appl. Phys.*, 2014, **47**, 030301.

This journal is © The Royal Society of Chemistry 2014

J. Mater. Chem. C, 2014, **2**, 4947–4956 | **4955**

3 G. L. Yuan, L. W. Martin, R. Ramesh and A. Uedono, *Appl. Phys. Lett.*, 2009, **95**, 012904.

4 Y. Sassa, M. Radovic, M. Mansson, E. Razzoli, X. Y. Cui, S. Pailhes, S. Guerrero, M. Shi, P. R. Willmott, F. Miletto Granozio, J. Mesot, M. R. Norman and L. Patthey, *Phys. Rev. B: Condens. Matter Mater. Phys.*, 2011, **83**, 140511.

5 E. Ertekin, V. Srinivasan, J. Ravichandran, P. B. Rossen, W. Siemons, A. Majumdar, R. Ramesh and J. C. Grossman, *Phys. Rev. B: Condens. Matter Mater. Phys.*, 2012, **85**, 195460.

6 A. Y. Borisevich, A. R. Lupini, J. He, E. A. Eliseev, A. N. Morozovska, G. S. Svechnikov, P. Yu, Y.-H. Chu, R. Ramesh, S. T. Pantelides, S. V. Kalinin and S. J. Pennycook, *Phys. Rev. B: Condens. Matter Mater. Phys.*, 2012, **86**, 140102.

7 D. Schumacher, A. Steffen, J. Voigt, J. Schubert, Th. Brückel, H. Ambaye and V. Lauter, *Phys. Rev. B: Condens. Matter Mater. Phys.*, 2013, **88**, 144427.

8 J. Rubio-Zuazo, L. Onandia, P. Ferrer and G. R. Castro, *Appl. Phys. Lett.*, 2014, **104**, 021604.

9 P. Bousoulas, I. Michelakaki and D. Tsoukalas, *J. Appl. Phys.*, 2014, **115**, 034516.

10 A. R. Silva and G. M. Dalpian, *J. Appl. Phys.*, 2014, **115**, 033710.

11 M. Choi, A. Janotti and C. G. Van de Walle, *Phys. Rev. B: Condens. Matter Mater. Phys.*, 2013, **88**, 214117.

12 R. Yang, S. Lin, X. Fang, X. Gao, M. Zeng and J. Liu, *J. Appl. Phys.*, 2013, **114**, 233912.

13 R. Vidya, P. Ravindran, H. Fjellvag, B. G. Svensson, E. Monakhov, M. Ganchenkova and R. M. Nieminen, *Phys. Rev. B: Condens. Matter Mater. Phys.*, 2011, **83**, 045206.

14 S. Lany and A. Zunger, *Phys. Rev. B: Condens. Matter Mater. Phys.*, 2010, **81**, 113201.

15 N. C. Giles, N. Y. Garces, L. Wang and L. E. Halliburton in *Quantum Sensing and Nanophotonic Devices: Proc. of SPIE, SPIE*, ed. M. Razeghi and G. J. Brown, Bellingham, WA, 2004, pp 267–278.

16 M. D. McCluskey and S. J. Jokela, *J. Appl. Phys.*, 2009, **106**, 071101.

17 J. Schneider and S. R. Sircar, *Z. Naturforsch., A: Phys., Phys. Chem., Kosmophys.*, 1962, **17**, 570.

18 A. Hausmann and H. Huppertz, *J. Phys. Chem. Solids*, 1968, **29**, 1369.

19 M. Diaconu, H. Schmidt, A. Pöppl, R. Böttcher, J. Hoentsch, A. Klunker, D. Spemann, H. Hochmuth, M. Lorenz and M. Grundmann, *Phys. Rev. B: Condens. Matter Mater. Phys.*, 2005, **72**, 085214.

20 S. S. Kim, J. H. Moon, B.-T. Lee, O. S. Sung and J. H. Je, *J. Appl. Phys.*, 2004, **95**, 454.

21 M. Lorenz, Pulsed laser deposition of ZnO-based thin films, in *Transparent Conductive Zinc Oxide. Basics and Applications in Thin Film Solar Cells (Springer Series in Materials Science vol. 104)*, ed K. Ellmer et al, Berlin, Springer, 2008, ch. 7, pp. 303–58.

22 H. Morkoc and Ü. Özgür, *Zinc Oxide: Fundamentals, Materials and Device Technology*, Wiley-VCG Verlag GmbH, 2009.

23 A. Janotti and C. G. Van de Walle, *Phys. Rev. B: Condens. Matter Mater. Phys.*, 2007, **76**, 165202.

24 T. Graf, M. Gjukic, M. Hermann, M. S. Brandt, M. Stutzmann and O. Ambacher, *Phys. Rev. B: Condens. Matter Mater. Phys.*, 2003, **67**, 165215.

25 M. Lorenz, C. Schmidt, G. Benndorf, T. Böntgen, H. Hochmuth, R. Böttcher, A. Pöppl, D. Spemann and M. Grundmann, *J. Phys. D: Appl. Phys.*, 2013, **46**, 065311.

26 Y. Zi-Yuan, *Chin. Phys. B*, 2009, **18**, 1253.

27 D. J. Newman and B. Ng, *Rep. Prog. Phys.*, 1988, **52**, 699.

28 W. L. Ju and M. G. Zhano, *Phys. Rev. B: Condens. Matter Mater. Phys.*, 1988, **37**, 9254.

29 W.-C. Zheng, S.-Y. Wu and J. Zi, *Z. Naturforsch., A: Phys. Sci.*, 2001, **56a**, 473.

30 V. A. Coleman and C. Jagadish, in *Zinc Oxide Bulk, Thin Films and Nanostructures*, ed. C. Jagadish and S. Pearton, Elsevier Ltd., 2006, pp. 1–20.

31 M. Grundmann, M. Scheibe, M. Lorenz, J. Bläsing and A. Krost, *Phys. Status Solidi B*, 2014, **251**, 850–863.

32 C. G. Ryan, *Nucl. Instrum. Methods Phys. Res., Sect. B*, 2001, **181**, 170.

33 L. Doolittle, *Nucl. Instrum. Methods Phys. Res., Sect. B*, 1985, **9**, 344.

34 S. Stoll and A. Schweiger, *J. Magn. Reson.*, 2006, **178**, 42.

4956 | *J. Mater. Chem. C*, 2014, **2**, 4947–4956

This journal is © The Royal Society of Chemistry 2014